Spontaneous Dynamics Predict the Effects of Targeted Intervention in Hippocampal Neuronal Cultures

Elisa Tentori[a,b], George Kastellakis[c], Marta Maschietto[b], Alessandro Leparulo[b], Panayiota Poirazi[c], Luca Mazzucato[a,d,e], Michele Allegra[a,e,*] and Stefano Vassanelli[a,b,*]

[a]Padova Neuroscience Center, University of Padua, Padua, 35129, Italy
[b]Department of Biomedical Sciences, University of Padua, Padua, 35131, Italy
[c]Institute of Molecular Biology and Biotechnology, Foundation for Research and Technology – Hellas (FORTH), Heraklion, 70400, Crete, Greece
[d]Departments of Biology and Mathematics and Institute of Neuroscience, University of Oregon, Eugene, 97403, Oregon, USA
[e]Department of Physics and Astronomy "G. Galilei", University of Padua, Padua, 35131, Italy

ABSTRACT

Achieving targeted perturbations of neural activity is essential for dissecting the causal architecture of brain circuits. A crucial challenge in targeted manipulation experiments is the identification of *high efficacy* perturbation sites whose stimulation exerts desired effects, currently done with costly trial-and-error procedures. Can one predict stimulation effects solely based on observations of the circuit activity, in the absence of perturbation? We answer this question in dissociated neuronal cultures on High-Density Microelectrode Arrays (HD-MEAs), which, compared to *in vivo* preparations, offer a controllable *in vitro* platform that enables precise stimulation and full access to network dynamics. We first reconstruct the *perturbome* - the full map of network responses to focal electrical stimulation - by sequentially activating individual single sites and quantifying their network-wide effects. The measured perturbome patterns cluster into functional modules, with limited spread across clusters. We then demonstrate that the perturbome can be predicted from spontaneous activity alone. Using short baseline recordings in the absence of perturbations, we estimate Effective Connectivity (EC) and show that it predicts the spatial organization of the perturbome, including spatial clusters and local connectivity. Our results demonstrate that spontaneous dynamics encode the latent causal structure of neural circuits and that EC metrics can serve as effective, model-free proxies for stimulation outcomes. This framework enables data-driven targeting and causal inference *in vitro*, with potential applications to more complex preparations such as human iPSC-derived neurons and brain organoids, with implications for both basic research and therapeutic strategies targeting neurological disorders.

Significance Statement. Neuronal cultures are increasingly used as controllable platforms to study neuronal network dynamics, neuromodulation, and brain-inspired therapies. To fully exploit their potential, we need robust methods to probe and interpret causal interactions. Here, we develop a framework to reconstruct the perturbome—the network-wide map of responses to localized electrical stimulation—and show that it can be predicted from spontaneous activity alone. Using simple, model-free metrics of Effective Connectivity, we reveal that ongoing activity encodes causal structure and provides reliable proxies for stimulation outcomes. This validates EC as a practical measure of causal influence in vitro. Our methodology refines the use of neuronal cultures for brain-on-a-chip approaches, and paves the way for data-driven neuromodulation strategies in human stem cell–derived neurons and brain organoids.

1. Introduction

Achieving precise and controlled perturbations of brain activity has been a longstanding goal in experimental neuroscience. Targeted perturbations can reveal how brain circuits process external stimuli [1, 2], assess the robustness of internal computations to external interference [3–5], uncover network-level mechanisms underlying neural computation, learning and dynamics [6–8], and allow closed- and open-loop control in brain-computer interfaces [6, 9, 10]. However, perturbation experiments *in vivo* encounter significant technical challenges, such as limited spatial resolution and difficulty in precisely targeting neuronal subpopulations. Dissociated neuronal cultures grown on High-Density Multi-Electrode Arrays (HD-MEAs) offer an accessible, yet biologically relevant experimental platform to overcome these limitations [11, 12]. *In vitro* cultures preserve key functional properties of neuronal circuits while simplifying their anatomical structure, thus enabling fine-grained manipulations that are difficult to achieve *in vivo*. These include precise spatial and temporal control over electrical stimulation and stable, high-resolution electrophysiological recordings [11], allowing for systematic probing of causal interactions across the network. Moreover, *in vitro* preparations provide highly reproducible conditions free from behavioral and systemic variability, and facilitate genetic and pharmacological manipulations that may be invasive or unfeasible in intact organisms [13]. These advantages make cultured networks particularly well-suited for testing

*Corresponding authors
michele.allegra@unipd.it (M. Allegra); stefano.vassanelli@unipd.it (S. Vassanelli)
ORCID(s):

and refining models of neural dynamics [14–17], developing targeted neuromodulatory strategies [18–20], and exploring core principles of neural computation and plasticity [21, 22] in a controlled and measurable setting.

In this work, we first develop a systematic protocol to obtain a detailed map of a neuronal culture's response to single-site, localized perturbations – referred to as "perturbome" in [23]. To this end, we adapt a framework originally developed for *in vivo* micro-stimulation studies in the primate prefrontal cortex [24] to the context of dissociated neuronal cultures. Our protocol systematically applies a sequence of localized perturbations on different sites of the culture, measuring responses across all recorded sites. This procedure enables us to estimate the pairwise *Interventional Connectivity* (IC; [24]) between different sites of the culture, defined as the strength of the response in site j caused by stimulation at site i.

However, such interventional mapping is resource-intensive, requiring repeated stimulation across many locations. To address this limitation, we investigate a second key challenge: predicting the impact of single-site perturbations purely from the network's spontaneous, unperturbed activity. To this end, we quantitatively compare IC with *Effective Connectivity* (EC), a framework for inferring directed interactions based on the ability of one unit's past activity to improve the prediction of another unit's future activity beyond its own history [25, 26]. Unlike structural connectivity, which reflects anatomical pathways, and Functional Connectivity (FC), which captures undirected statistical dependencies, EC explicitly characterizes causal influences [27, 28].

Various methods have been developed to infer EC from spiking data, typically using statistical or information-theoretic approaches to estimate directional interactions from spontaneous activity recordings. However, the extent to which EC estimates truly reflect causal interactions remains unclear. Most validation studies rely on *in silico* simulations, where inferred EC is compared to a known structural ground truth [26, 29–35]. Yet, this approach has critical limitations: first, simulations inevitably simplify biological mechanisms, potentially leading to overoptimistic performance [36]; second, structural connectivity does not represent a valid ground truth for EC, since causal interactions emerge from dynamic processes that are only partially constrained by anatomy [23, 37]. By comparing EC and IC directly from experimental data, we aim to both evaluate the predictive power of EC and assess its validity as a proxy for causal influence. Specifically, we compare IC with three EC metrics: delayed Transfer Entropy (TE) [26, 38], a model-free, information-theoretic measure capturing nonlinear directed interactions between spike-trains; Signed Cross-Correlation (SC) [35], a cross-correlation-based measure identifying directional inhibitory and excitatory interactions by correcting spike coincidences for chance-level occurrences; and Cross-Covariance (XCov), which captures linear, time-lagged dependencies between spike trains, relative to those expected under independence. By systematically comparing EC with IC, we show that EC metrics provide robust and reproducible estimates of directed interactions, capable of reliably predicting perturbation outcomes. This demonstrates their practical utility for guiding targeted neural modulation and supports their use as a scalable framework for causal mapping *in vitro*.

2. Results

To test whether EC metrics inferred from spontaneous activity can predict the impact of single-site perturbations, we designed a two-phase experimental protocol on dissociated rat hippocampal cultures plated on HD-MEAs. In the first phase, we recorded $T_{rec} = 30$ minutes of spontaneous spiking activity from $N = 1024$ electrodes and estimated EC using three complementary metrics: TE, SC, and XCov. In the second phase, we applied a train of biphasic electric pulses ($T_{\text{stim}} = 120$ ms; amplitude: 300 mV; frequency: 200 Hz) to a subset of $M = 20$–25 stimulation channels, one at a time, across $N_T = 200$ randomized trials. The stimulation sequence was reshuffled at each trial, so that all M channels were stimulated once per trial in a randomized order (see Section 4.3 for details). Neural activity was recorded across the entire N-channel array before and after each stimulation, enabling the measurement of network responses to isolated perturbations. For each stimulation–recording pair ($i \rightarrow j$), we quantified IC as the Kolmogorov–Smirnov distance between pre- and post-stimulation spike-count distributions across trials. The resulting $M \times N$ IC matrix captured the directed effect of each localized intervention — effectively mapping the culture's *perturbome* [23]. This perturbome provides an empirical benchmark against which to evaluate the predictive accuracy of EC metrics inferred from spontaneous dynamics.

In what follows, we first characterize the perturbome: we analyze the spatial and temporal structure of stimulation-induced effects, and highlight how responses vary across the network. We then evaluate the predictive power of EC in explaining these effects, assessing how well different EC metrics reconstruct the IC matrix. Finally, we disentangle the contributions of spatial proximity and network topology to the EC–IC relationship, and explore which features of EC best account for stimulation outcomes.

Experiments were conducted on two cultures. Unless otherwise specified, figures refer to one representative culture exhibiting two spatially segregated clusters. Summary statistics across both recorded cultures are provided in the Supplementary Information.

2.1. Spatial Features of Perturbation Effects

We first examined how single-site perturbation shaped network responses across space. Despite their short duration, stimulations consistently induced marked changes in neuronal firing, with effects tightly dependent on the specific source–target pair (Figures 2b and 2c). Responses were reproducible across trials and heterogeneous across the array: some sites exhibited excitation followed by suppression, others showed purely inhibitory effects, and several remained

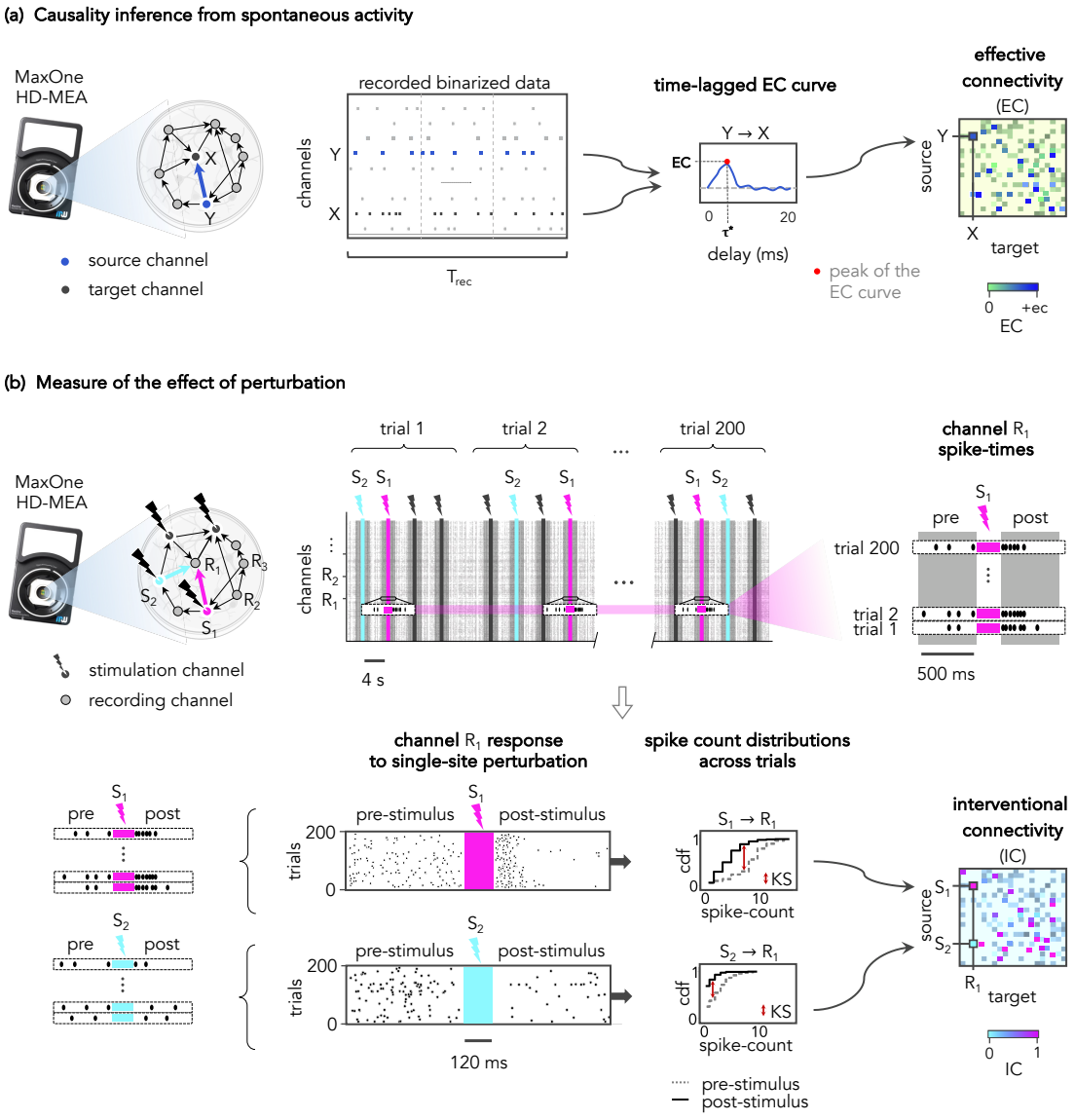

Figure 1: Experimental protocol for validating EC inference methods through comparison with IC. **(a)** Causality inference from spontaneous activity. In the first phase, spontaneous neural activity is recorded for $T_{rec} = 30$ minutes from a subset of highly active channels ($N \approx 1024$) selected from the MaxOne HD-MEA chip. The recorded spike data (binarized, middle panel) is used to compute delayed EC metrics, which quantify directed causal interactions between pairs of channels (e.g., $Y \rightarrow X$). EC values computed across all channel pairs yield a source-by-target connectivity matrix (right panel). **(b)** Measurement of the network responses to perturbations. In the second phase, the network's response to single-site perturbations is experimentally measured to derive IC. **Top left panel:** Each selected stimulation channel (e.g., S_1, S_2) is individually stimulated across multiple trials ($N_T = 200$), and neuronal activity is recorded simultaneously from all channels in the map (recording channels, e.g., R_1, R_2). **Top central panel:** An example raster plot of spike-times (black dots) recorded simultaneously across multiple recording channels for consecutive trials. Colored (pink, cyan) or black stripes indicate stimulation intervals, where stimulation is delivered in randomized order to the stimulation channels; pre- and post-stimulation intervals used for IC analysis are shaded in light gray. Each trial block includes a pre-stimulation recording interval (light gray), a stimulation interval ($T_{stim} = 120$ ms, 300 mV, 200 Hz pulse-train; indicated by colored stripes for selected channels, dark gray for other stimulated channels), and post-stimulation recording. **Top right panel:** Spikes recorded from a single target channel (R_1) pre- and post-stimulation of a given channel (e.g., S_1) are grouped across trials This grouping procedure is repeated for each stimulation–recording channel pair. **Bottom central panels:** Two examples of grouped spike responses from the same recording channel (R_1): the upper raster plot shows an excitatory response (increased spiking activity) followed by inhibition in response to stimulation of channel S_1 (pink), while the lower raster plot illustrates a predominantly inhibitory response following stimulation of channel S_2 (cyan). Responses are consistent across multiple trials. The spike counts from pre- and post-stimulation windows are used to construct empirical distributions and their corresponding cumulative distribution functions (cdfs). The causal effect on R_1 of the stimulations of S_1 and S_2 is computed through the Kolmogorov–Smirnov (KS) distance between the pre- and post-stimulus cdfs (ranging from 0 to 1), which defines the IC metric. **Bottom right panel:** IC values computed across all stimulated and recorded channel pairs produce the IC matrix (bottom right panel). The predictive power of EC is validated by evaluating the correspondence between the spontaneous-activity-based EC and the perturbation-based IC matrices.

unaffected. This diversity reflects the structure of the underlying network. For example, channel 728 (Figure 2c, left panel) responded to stimulation from electrodes such as, e.g., 772, 660, and 302 with an initial increase in firing followed by inhibition, whereas stimulation from channels 696, 600, and 212 predominantly evoked only suppression. Such differences likely reflect the interplay of direct excitatory inputs activated by stimulation and network-mediated inhibitory feedback loops. Specifically, an initial increase in firing may result from direct excitation of connected neurons, whereas

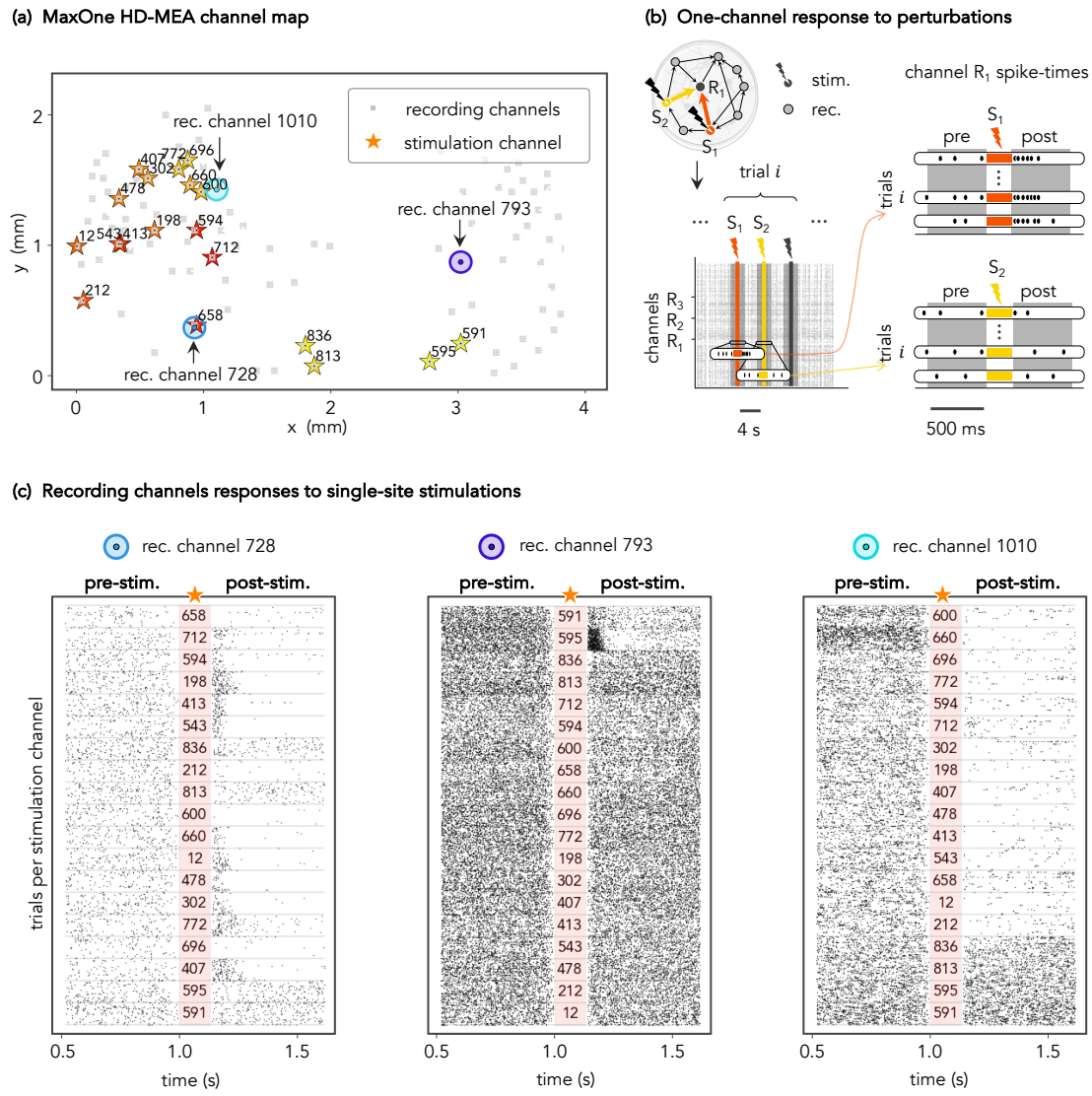

Figure 2: Spatial and temporal effects of perturbation across recording channels 728, 793 and 1010. **(a)** N-channel map, selected from a 26,400-electrode grid based on the most active areas on the HD-MEA. Recording channels, marked with light-grey squares, are clustered into left and right groups, reflecting two spatially segregated zones on the chip. The set of $M = 19$ stimulation channels are highlighted with yellow stars and labeled with their IDs. The three representative recording channels analyzed in detail (728, 793, and 1010) are indicated by blue, light blue, and turquoise circles, respectively. **(b)** Schematic representation of the second phase of the experiment (perturbation-response characterization). After selecting the stimulation channels (illustrated as S_1 and S_2 in the network), an alternating stimulation-recording protocol was implemented (lower-left panel), delivering stimulation to individual channels in randomized order across $N_T = 200$ blocks (or trials). During post-processing, responses to each stimulation channel were grouped across trials (the right panel shows two examples of the trial-aligned responses recorded from channel R_1 to stimulation in channels S_1 and S_2). **(c)** Neural activity from channels 728, 793, and 1010 (left, central, right panels) in response to perturbations from each stimulation electrode. Each raster plot displays spike times segmented into 500 ms pre-stimulation, 120 ms stimulation (indicated by pink shading), and 500 ms post-stimulation periods, over N_T trials organized vertically by stimulation channel. Raster plots are sorted according to the increasing distance between stimulation and recording channels. Stimulation electrodes are indicated explicitly by their channel IDs on the pink shade. This multi-trial representation highlights the spatial gradient and temporal consistency of perturbation effects, revealing distinct response patterns, including excitation followed by inhibition, primarily inhibitory responses, or absence of response, depending on the specific stimulation-recording channel pair.

the subsequent suppression could be mediated by recurrent activation of inhibitory interneurons or activity-dependent adaptation mechanisms.

Spatial organization of responses revealed two key aspects. First, perturbation effects decayed with distance: stimulation most strongly influenced nearby channels, tending to diminish as the distance from the stimulation site increased. Second, responses were shaped by the network's modular structure. The recording map (Figure 2a) revealed two spatially segregated clusters (a characteristic of the specific culture analyzed here, chosen explicitly to illustrate the potential of our approach). Source-to-target influence patterns showed strong intra-cluster coupling and weak inter-cluster communication, highlighting limited inter-cluster communication and the presence of two distinct, internally cohesive regions. Stimulations within a cluster (e.g., channel 595 on the right) primarily modulated nearby targets within the same cluster (e.g., channel 793), with little to no effect on neurons in the opposite cluster (e.g., channels 728, 1010).

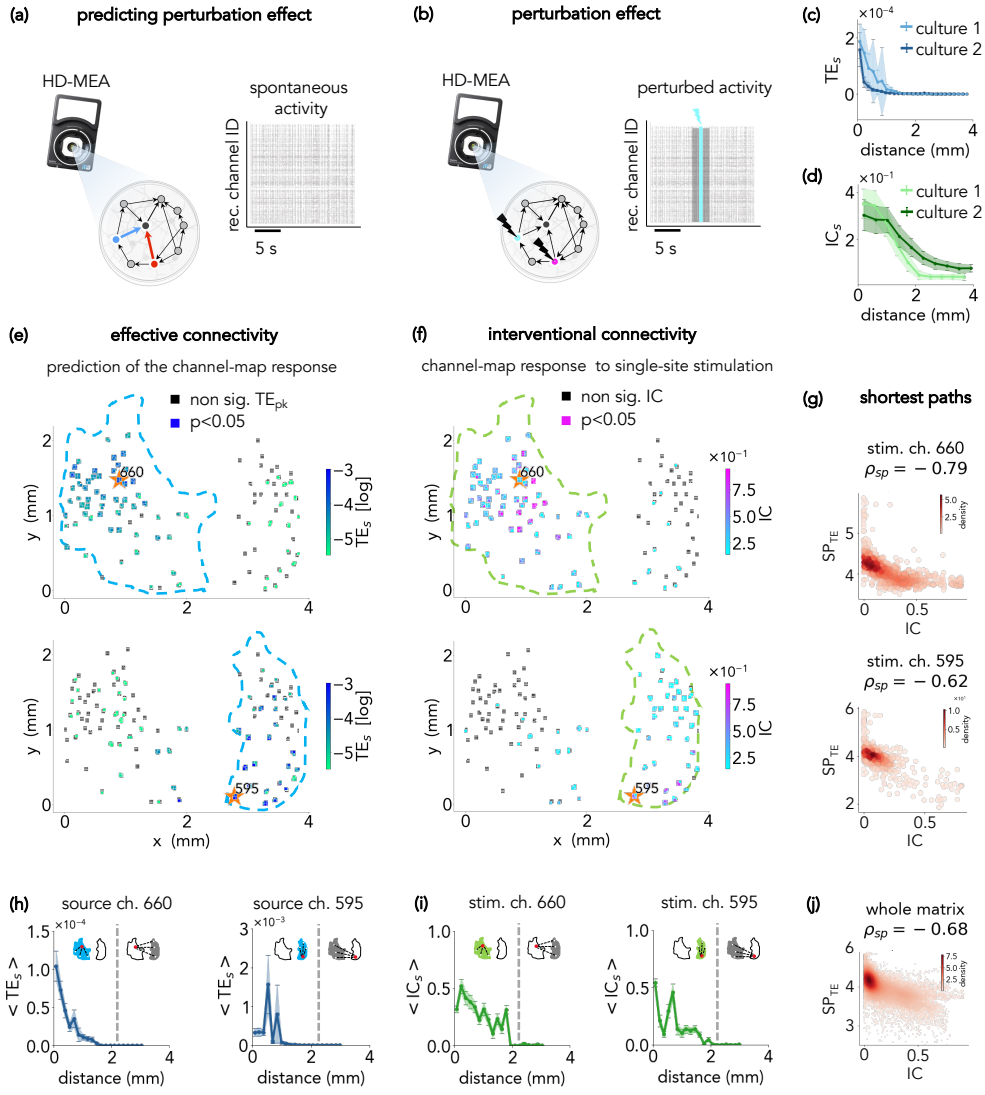

Figure 3: **(a)** Schematic illustration of EC estimation from spontaneous activity. Example raster plot of spontaneous spiking activity recorded from Culture 1, used to infer EC (right). Spikes are shown as black dots; rows represent the spike-trains of specific recording channels, ordered by ID. **(b)** Schematic illustration of perturbation experiments used to measure IC. Raster plot of neural responses recorded during the stimulation protocol (right); each row corresponds to a recording channel ordered by channel ID. Vertical cyan bar indicates the brief stimulation event (120 ms). **(c-d)** Spatial profiles showing mean EC quantified by TE (upper panel) and mean IC (lower panel), as a function of inter-electrode distance. Each panel displays curves corresponding to Culture 1 and Culture 2, revealing consistent distance-dependent decay in both TE and IC metrics. Error bands represent standard error of the mean (s.e.m.). **(e)** Two representative examples of predicted perturbation effects derived from spontaneous-activity-based EC (computed using TE). Each square represents a recording channel, spatially arranged according to the HD-MEA electrode map. Colors indicate the EC strength (log-scale TE values) between the assumed source channel (orange star; top panel: channel 660, bottom panel: channel 595) and each recording channel (target). Non-significant EC links (jittering test, $p > 0.05$) are shown in black. TE predictions reveal spatially structured responses, accurately identifying functional clusters (blue dashed lines) and capturing the spatial gradient of connectivity observed experimentally (see panel f). **(f)** Corresponding experimentally measured perturbation responses (IC) following single-site stimulation from the same electrodes as in panel **e** (top panel: channel 660, bottom panel: channel 595). Colors indicate IC values, calculated as the Kolmogorov-Smirnov distance between pre- and post-stimulation spike-count distributions. Stimulated channels are highlighted by an orange star. Non-significant perturbation effects ($p > 0.05$) are shown in black. IC reveals source-specific patterns, spatially clustered (green dashed lines). Perturbation effects exhibit spatial gradients that progressively decay with distance from the stimulation site. **(g)** Density scatter plots illustrating the relation between IC and the SP computed from the TE-inferred network, using Dijkstra's algorightm, with distances defined as the inverse of TE weights. Top and bottom panels show results for stimulation channels 660 and 595, respectively, with corresponding Spearman correlation coefficients (ρ_{sp}). **(h)** Spatial footprint of the mean TE as a function of distance for source channels 660 and 595 (respectively left and right panel). EC reconstruct the clustered organization of the responses and the decreasing of the response as a function of distance. **(i)** Spatial profile of mean IC as a function of distance from stimulated channels 660 (left panel) and 595 (right panel). Average response strength decreases with distance, approaching zero for inter-cluster distances. The curves' errors were calculated as the s.e.m. of the measure. **(j)** Density scatter plot of shortest path lengths (from TE) versus IC values computed across all stimulation channels (entire $M \times N$ matrix) from Culture 1. A clear negative correlation ($\rho_{sp} = -0.68$) emerges, demonstrating the predictive capacity of shortest paths computed from EC to capture network-wide perturbation effects.

Conversely, stimulation from the left cluster strongly affected 728 and 1010, but not 793. Nonetheless, exceptions to this spatial rule were observed: certain stimulations occasionally elicited strong responses in distant targets, suggesting an inhomogeneous circuit structure where some connections bypass typical geometric constraints. The spatiotemporal structure of perturbation effects reflects a combination

of local influence, modular topology, and heterogeneous connection strengths.

2.1.1. Spatial Features of Interventional Connectivity

We next examined the spatial structure of the perturbome, as captured by the IC metric, which summarizes the causal impact of each stimulation site on all recording channels (Figure 3b).

IC values exhibited a clear spatial gradient: perturbation effects decayed with increasing distance from the stimulation electrode (Figure 3d), a trend consistent across both analyzed cultures [Culture 1 and Culture 2 in figure], indicating that physical proximity plays a key role in shaping perturbation impact.

A clustered organization also emerged. In the representative culture shown (Figure 3f), stimulation from the left cluster (e.g., channel 660) predominantly modulated nearby targets within the same cluster, with little effect on the opposite cluster (Figure 3f, top). The reverse was true for stimulations from the right cluster (e.g., channel 595, bottom). Within clusters, perturbation effects remained distance-dependent but varied in strength (Figure 3i). Within each cluster, effect magnitude remained distance-dependent but highly heterogeneous (Figure 3i), with a Gini coefficient of 0.51 ± 0.03 across stimulation-sites, reflecting a small number of strong influences amid many weaker ones. These features reveal a perturbome shaped by spatial gradients, modular topology, and uneven connection strengths — pointing to a network architecture where localized, hierarchical influences dominate.

2.2. Predicting Stimulation Effects from Spontaneous Activity

To evaluate whether EC can predict how the network responds to perturbations, we estimated EC from spontaneous activity recorded prior to the perturbation experimental phase. Cultures displayed characteristic bursting dynamics (Figure 3c), with mean firing rates between 0.5 and 5 Hz and bursts occurring at $0.5 - 1$ Hz. EC was computed over the entire 30-minute spontaneous recording window ($T_{\text{rec}} =$ 30 min), maximizing statistical power and reducing noise. Results from shorter recordings were consistent and reported in Supplementary Information B. Here, we focus primarily on peak-based ("pk") metrics (TE, SC, and XCov), which consistently outperformed alternative versions (z-scored and Coincidence Index-based variants, reported in Supplementary Information C).

2.2.1. Predicting Spatial Footprint

We first tested whether EC — which reconstructs causal links from spontaneous activity — captures the spatial structure of the perturbome. Since each stimulation site used for IC estimation corresponds to a source node in the EC matrix, we directly compared the row of EC values from a given source to its corresponding IC vector.

All three pk-based EC metrics recovered the spatial footprint of IC remarkably well. EC values decreased with distance from the source, in line with the spatial decay observed in IC (Figure 3c-d). However, while IC decayed roughly linearly with distance, EC values showed a sharper exponential drop-off (see TE example in Figure 3h vs. IC in 3i). Among the three, TE produced the sharpest decay and cleanest spatial segregation, removing most long-range connections across clusters when significance testing was applied (Figure 3e). EC maps also reproduced the modular organization of the perturbome: stimulation from a site within one cluster yielded strong EC values to nearby sites within the same cluster and much weaker or absent values across clusters (Figure 3e vs. 3f). Applying significance thresholds to the EC matrix further enhanced this spatial specificity, particularly for TE and SC [see also Figure S10 and Figure S11, right panels, illustrating other examples for spatial clustering recovered by significant connections of SC and XCov, and the barplots in Figure 4e and 4f].

Connection strength distributions in the EC matrices were highly skewed. Across all three pk metrics, Gini coefficients were consistently high (TE: 0.73 ± 0.07; SC: 0.66 ± 0.07; XCov: 0.66 ± 0.06), reflecting a small number of strong links amid many weak ones. This sparsity aligns with the heterogeneous IC responses and suggests a shared underlying topology.

Finally, the mean TE profile as a function of distance closely mirrored the IC profile, especially in the tail (Figure 3g-i), supporting the idea that EC can predict the spatial gradient of stimulation-induced effects. All three pk-based EC metrics reproduce the spatial organization and modularity of the perturbome. Comparisons with SC and XCov are reported in the Supplementary Material. A z-scored version of these three EC measured was still predictive of the IC but less significant than the raw measures.

2.2.2. Indirect Connectivity Captures Perturbation Spread

We asked whether the pattern of stimulation-induced responses — as measured by IC — could be explained not only by direct (possibly monosynaptic) EC links, but also by indirect routes in the EC network. To test this, we computed Shortest Path (SP) distances from the full $N \times N$ EC matrix, using the inverse EC weight as functional distance (see Section 4.4.8). This yielded, for each source–target pair, the most efficient path of influence, potentially involving polysynaptic steps. The resulting SP matrices were then reduced to $M \times N$ to match the IC format.

For all the metrics, SP values were anticorrelated with IC across both cultures: the shorter the functional path from a stimulation site to a recording channel, the stronger the perturbation effect (Figure 3j). This held consistently across individual source channels (Figure 3g), indicating that IC reflects both direct and indirect functional connectivity. The distinct spatial decay profiles of EC and IC support this interpretation. EC values dropped exponentially with distance, consistent with sensitivity to local, direct interactions. IC decayed more gradually, approximating a linear trend, suggesting that stimulation effects accumulate over multiple, possibly weak, links. This points to a distributed mechanism

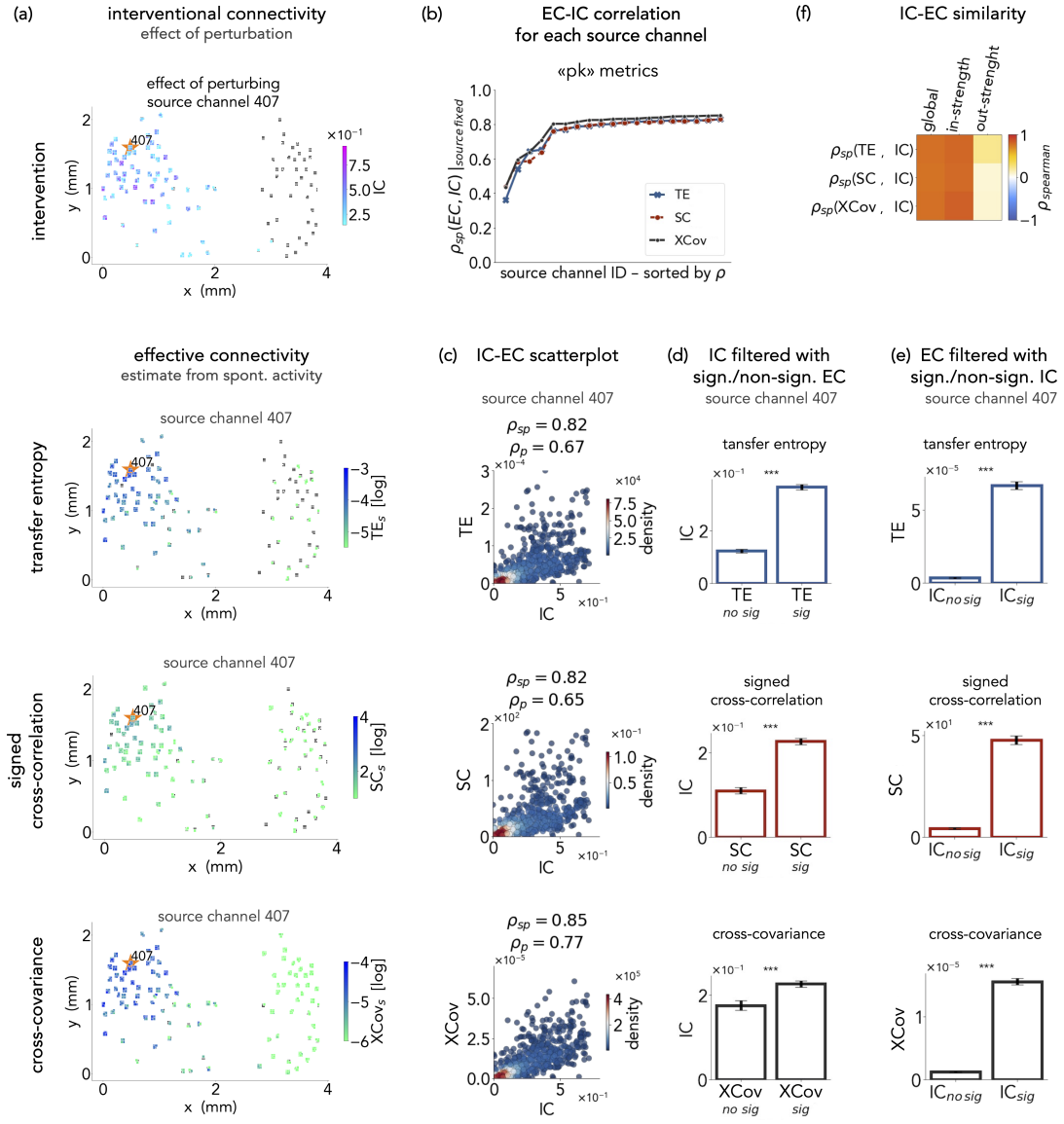

Figure 4: How EC derived from spontaneous activity predicts stimulation-induced effects. **(a)** Top panel: IC map for a representative source electrode (channel 407), showing significant responses across the array. Lower panels: Corresponding EC maps obtained using TE, SC, and XCov (non-z-scored). **(b)** Reconstruction accuracy (ρ_{sp}) for all source electrodes, comparing IC to each EC measure (pk; [results for pk-CI and z-scored pk-CI in Supplementary Information 4.4.9]). Each curve represents one measure and is sorted to ensure a monotonic increase in accuracy values. **(c)** Scatter plots of IC vs. TE, SC, and XCov (non-z-scored) for source channel 407, illustrating a strong positive correlation. **(d)** Mean EC values for source-target pairs grouped by whether their IC effect is significant (right bar in each pair) or not (left bar). **(e)** Mean IC values for source-target pairs grouped by whether their EC link is significant (right bar in each pair) or not (left bar). The analyses in **(d)** and **(e)** are shown separately for TE, SC, and XCov. Error bars represent the standard error of the mean (s.e.m.). A permutation test was applied for significativity, with null ipothesis that the mean values of the two bars were identical. Asterisks $*$, $**$, $***$ indicate significance levels of $p < 0.05$, 0.01, and 0.001, respectively. **(f)** Reconstruction accuracies calculated on full IC-EC matrices (left column in the matrix), as well as in-strength (central column) and out-strength (right column) distributions.

of influence, where the perturbation propagates along the most efficient functional routes, not merely through nearest-neighbor or strongest connections. While the main figures show results for TE, the same relationship holds for SC and XCov.

2.2.3. *Single-site Predictions*

We next quantified how well EC predicts stimulation-induced effects by correlating, for each stimulation site, its EC vector with the corresponding IC vector. Agreement was measured via Spearman correlation (ρ_{sp}). We termed this metric "reconstruction accuracy", because it quantifies how well stimulation-induced changes (IC), defined by pre- and post-stimulation differences in spike count distributions, can be inferred from spontaneous activity patterns (EC). Since IC is derived from a two-sided Kolmogorov-Smirnov test (see Section 4.3.2, it identifies whether post-stimulation activity distribution significantly differs from baseline without specifying the direction of change (i.e., wether the activity increases or decreases). Consequently, IC cannot distinguish between excitatory and inhibitory effects. To enable a direct comparison with EC metrics that include sign (i.e.,

distinguishing excitatory and inhibitory links), we took the absolute values of EC estimates.

Across source channels, "pk" measures (hereafter referred to as "pure") achieved the highest reconstruction accuracy (across source channels, $< \rho_{sp} >= 0.76 \pm 0.12$ for TE, $< \rho_{sp} >= 0.75 \pm 0.11$ for SC, and $< \rho_{sp} >= 0.79 \pm 0.11$ for XCov), as shown in Figure 4b. In contrast, z-scored versions yielded lower ρ_{sp} values, while "CI" measures consistently underperformed compared to their "pk" counterparts (Figure S13,S14) [a complete overview of the "pk" and "CI" results is provided in Supplementary Information C]. As the "CI" versions of TE, SC, and XCov, in general, consistently underperform compared to their "pk" counterparts, both in pure and z-scored implementations, their discussion is omitted from the main text and left for reference in the Supplementary Information. Among the "pk" measures, XCov exhibited slightly higher correlations compared to TE and SC. However, the performance of all three measures was comparable and consistently high, with ρ_{sp} exceeding 0.8 for most source channels (see an example in Figure 4c). Critically, all pure "pk" EC measures mirror the stimulation outcomes, showing strong values where perturbation effects are significant, and weak values where responses are non-significant (Figure 4d). Conversely, non-significant EC connections corresponded to weaker IC values, and significant ones were more likely to display measurable IC effects (Figure 4e).

Interestingly, all the "pk" measures exhibit match the firing rates profile (Figure S17): source-target channels with higher activity have stronger EC [mean Pearson correlation across source channels $< \rho_p >= 0.18 \pm 0.10$, 0.23 ± 0.10 and 0.29 ± 0.09 respectively for TE, SC and XCov], compared to z-scored analogues [$< \rho_p >= 0.12 \pm 0.09$ for all measures]. While pure measures are influenced by firing rates, this dependency appears to reflect genuine network organization rather than a trivial artifact, as supported by the similar rate dependence of IC ($< \rho_p >= 0.36 \pm 0.06$). As suggested by previous studies [30], this rate dependency may reflect a neuron's true influence on the network, implying that EC's sensitivity to firing rate contributes to its ability to predict stimulation effects, as independently confirmed by IC.

Furthermore, the enhanced ability of pure "pk" measures to reconstruct IC was confirmed through global analyses (Figure 4f). Reconstruction accuracy was assessed for entire EC and IC matrices, revealing that non-z-scored measures consistently outperformed the others in capturing overall network connectivity. Additionally, comparisons of in- and out-strength distributions between EC and IC highlighted the robust predictive performance of pure "pk" measures, reinforcing their efficacy in mapping the network's causal structure (see also Figure S13 in Supplementary Information C).

2.2.4. Correcting for Spatial Dependency

Both the EC measures and the perturbation effects exhibited spatial decay relative to the source electrode. To determine whether the predictive relationship between EC and IC was solely driven by spatial proximity, we performed a partial correlation analysis by removing the spatial dependence from the connectivity values. Specifically, we modeled the decay in IC and EC as a function of the inter-electrode distance $\mathbf{d}$ by fitting it with an exponential function (Figure 5a,b) (see Section 4.4.9 for details). The residuals of the fit, $\epsilon_{\mathbf{IC}}$ and $\epsilon_{\mathbf{EC}}$, representing the detrended connectivity values, were then used to test whether the relationship between EC and IC persisted after removing spatial decay. To this end, we applied the spatial correction independently to each source channel i by fitting the corresponding row of the connectivity matrices for both IC and the EC measures. The reconstruction accuracy was subsequently quantified as the Spearman correlation coefficient between the residuals, $\rho_{sp}(\epsilon_{\mathbf{IC_i}}, \epsilon_{\mathbf{EC_i}})$.

We then tested whether higher EC values corresponded to larger IC values in target clusters compared to channels with no significant EC, even after correction. As shown in Figure 5c-f, in a specific example for TE at fixed source channel, this was indeed the case: before correction, target clusters with significant TE exhibited higher IC values, while those with non-significant TE displayed lower IC values (Figure 5c,d). After correcting for spatial dependency, the relationship remained robust, with significant TE values still associated with higher IC values (Figure 5e,f). These findings were consistent across all tested source channels and for all "pk" EC measures, as shown in Figure 5g. Although the spatial correction reduced the magnitude of the correlations, the non-z-scored "pk" measures retained high predictive power, confirming that the relationship between EC and IC extends beyond the effects of spatial decay.

2.2.5. Connection Probability as a Function of Distance

We next analyzed how the probability of significant causal connections varies as a function of inter-channel distance. Distances were divided into bins of 0.04 mm, and the connection probability was calculated as the fraction of significant connections relative to all possible connections within each bin. This analysis was conducted for both the IC matrix and the corresponding EC matrices. The results, shown in Figure 5a,b (right panels), reveal a clear divergence in the spatial decay of connection probability between IC and EC measures. Specifically, the connection probability for non-z-scored TE declines exponentially with distance, suggesting that TE predominantly captures local, direct causal interactions. In contrast, the probability of significant IC connections decreases more gradually, exhibiting a near-linear trend that likely reflects the influence of longer-range, potentially indirect or modulatory processes. This finding is consistent with the trends in IC and TE values as a function of distance previously described (Figure 5a,b, left panels). These differences may also stem from the nature of the two measures. EC estimates, being probabilistic, are inherently more sensitive to signal strength and noise, whereas IC provides a direct experimental measure of network activity.

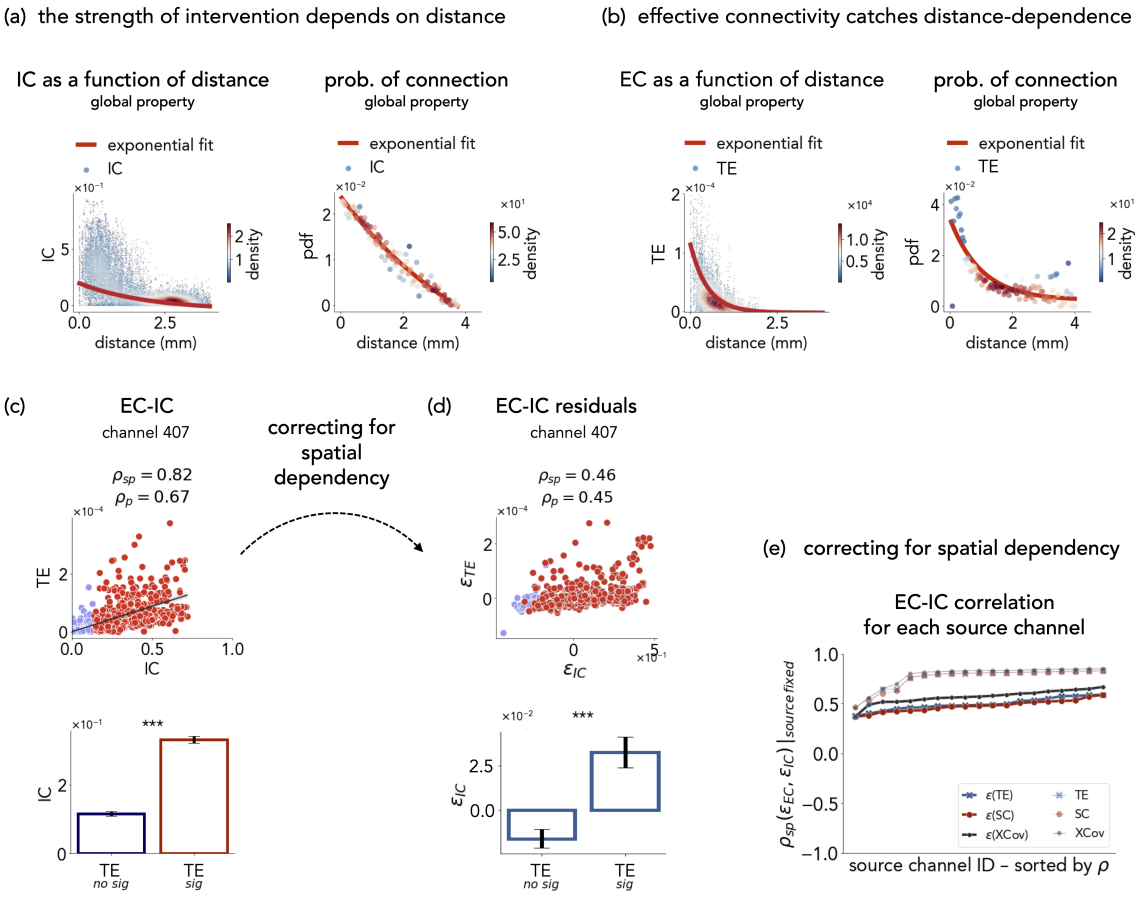

Figure 5: EC predictions corrected for spatial dependency. **(a)** IC as a function of distance. **Left panel:** IC's links scattered as a function of distance and fitted with a decreasing exponential. In the scatterplot, the colormap scale with the point density. **Right panel:** Probability of significantly influencing the activity of a channel with perturbation, as a function of distance. Distance was divided into bins of 0.04 mm, and probability was calculated as the frequency of significant connections relative to all possible connections at a given distance. **(b)** TE exponentially decaying with distance. **Left panel:** TE links fitted with a decreasing exponential with distance. **Right panel:** Probability that two channels are significantly causally connected as a function of their distance. **(c)-(d)** Relationship between TE and IC before correcting for spatial dependency, for fixed source channel 407. **(c)** TE-IC relation, with Spearman and Pearson correlations highlighed (ρ_{sp} and ρ_p respectively). Higher TE source-target links correspond to the ones significantly affected by perturbation (IC). In the scatterplot, red (violet) dots correspond to significant (non-significant) IC links. **(d)** For significant TE, perturbation effects are on average higher that for non-significant TE. Error bars represent the standard error of the mean (s.e.m.). Asterisks $*$, $**$, $***$ indicate significance levels of $p < 0.05$, 0.01, and 0.001, respectively (permutation test). **(e)-(f)** Relationship between the residuals of TE and IC after correcting for spatial dependency, for fixed source channel 407. **(e)** Relation between TE and IC residuals after correction. **(f)** Mean residual IC maintain higher values when TE is significant. **(g)** Reconstruction accuracy of EC metrics corrected for spatial dependency, measured as the Spearman correlation coefficient between the residuals of the EC and IC fits.

The observed spatial trends align with established findings across neural systems, spanning from macroscopic brain networks to local circuits. In such systems, the connection probability typically decays with distance, reflecting both the energetic costs of maintaining long-range connections and the spatial density of neural wiring. Importantly, these results were consistent across all "pk" and "CI" measures, supporting the robustness of EC metrics in capturing the topological constraints governing signal transmission. The persistence of significant IC connections at larger distances suggests that IC captures network dynamics that are less constrained by spatial proximity, potentially reflecting indirect or modulatory interactions or direct long-range projections. In contrast, the sharper decay observed for EC measures, such as TE, may underscore their sensitivity to local causal interactions.

3. Discussion

In vitro recordings with Micro-Electrode Arrays (MEAs) provide a fully controlled experimental environment to study the formation and development of neuronal circuits, as well as their response to a wide array of electrical and chemical manipulations. The recent advent of HD-MEAs with fine spatial resolution, such as the Max-One array, enables a precise sampling of the neuronal population under investigation and stimulation of single cells or small groups of cells with high precision [12], offering unprecedented opportunities for spatially targeted perturbations. In this work, we presented a framework for predicting the effects of targeted electrical perturbations in primary neuronal cultures coupled with HD-MEAs, based on causal interactions inferred from spontaneous spiking activity. Our findings demonstrate that single-site stimulation effects on network-wide activity can be accurately captured using EC estimates derived from

spontaneous activity, leveraging measures such as TE, SC and XCov. Building on this two-stage protocol, we outline three key contributions. First, we adapt and apply the IC framework recently introduced *in vivo* by [24] to dissociated neuronal cultures coupled with HD-MEAs. We show that the perturbome — the directed map of stimulation-induced effects — can be robustly and reproducibly reconstructed *in vitro*, across trials and stimulation sites. This establishes the applicability of the framework to controlled, high-resolution systems. Second, we show that spontaneous activity in cultured neuronal networks encodes the circuit's causal structure, and can be used to predict the perturbome in advance. EC measures computed from spontaneous spiking accurately track the spatial footprint and strength of perturbation-induced effects. This enables a shift from trial-and-error to data-driven stimulation targeting and highlights its potential for *in vitro* neuromodulatory strategies [39–43] or the optimization of BCIs. Third, we systematically compare estimation strategies — including TE, SC and XCov — across different normalization schemes, and identify a subset of metrics that reliably track the perturbome. Among these, SC emerges as a simple, computationally efficient and robust option for dissociated neuronal populations. Finally, we release an open-source software suite that implements the entire pipeline — from IC estimation to EC estimation and validation — enabling reproducibility and extension to other systems, such as stem cells and cortical slices. Together, our methodology provides a relevant technical advance in the search for precise, circuit-specific manipulations in neuronal cultures, with broad implications for experimental and clinical neuroscience *in vitro* and the perspective of implementing an online scan protocol.

The IC framework introduced by Nejatbakhsh et al. [24], originally applied *in vivo* to the macaque cortex using 96-channel Utah MEAs, was based on a powerful and simple protocol: single-site electrical perturbations delivered across multiple randomized trials, and responses measured as pre–post differences in firing statistics. Here, we translate and extend this framework to dissociated hippocampal cultures plated on HD-MEAs, enabling stimulation and recording at high spatial resolution across one thousand of electrodes. As a first contribution, we show that the perturbome — the matrix of causal effects elicited by stimulation — can be robustly reconstructed *in vitro*. Responses are highly reproducible across trials (Figure 2) and stimulation sites, as confirmed by cross-validating the IC matrices obtained from independent trial subsets (see Supplementary Information B.1). Moreover, the resulting perturbation patterns exhibit high spatial specificity, typically confined to the local network surrounding the stimulation site, but also including consistent long-range effects in specific configurations. This specificity of perturbation effects supports the suitability of the IC protocol for fine-scale causal mapping *in vitro*, underscoring the ability of targeted stimulation to perturb the network in a spatially well-controlled manner. While extensive research has focused on how temporal properties of stimulation, such as frequency, affects the network responses [39–41, 43, 44], the literature features hardly any thorough analysis of the spatial degrees of freedom in the choice of where to stimulate, except in the case of extremely controlled scenarios where the geometry of the network is externally controlled [14, 45]. We found that stimulation of a single channel determines responses that are quite diverse across recording channels, whose profiles include sudden rise in activity followed by activity suppression; inhibitory responses; or no responses (Figure 2c). While the absence of a response can be easily interpreted (non existence of a causal path between the two channels), the other two behaviors are more subtle. The sudden rise in activity followed by low activity could emerge from excitation provided by the stimulated channels, with a feedback mechanism provoking the activity suppression. Fully suppressive responses suggest a recurrent inhibition process where (unobserved) inhibitory neurons are strongly excited by the overall network response, then providing inhibitory feedback. An alternative explanation would be that single cells are capable of short-term adaptation of their firing rate. At present, we cannot offer a conclusive interpretation: more light could be shed on the mechanisms at play by repeating the experiment while selectively blocking excitation or inhibition by administering proper compounds [46]; by simultaneous calcium imaging recordings of cell-type specific populations; or by optotagging of inhibitory neurons [47].

A second key contribution is the possibility to use spontaneous recordings to predict the effect of interventional stimulation. This possibility is encapsulated in the level of agreement found between EC and IC. We tested three common EC metrics, along with several normalization strategies proposed in the literature. We found that the vanilla (unnormalized) versions of the EC metrics give the best similarity with IC, with little difference between the measures used (Figure 4). For most stimulation channels, the agreement between EC and IC gives a Spearman coefficient > 0.8, which implies that the ranking of EC links is strongly predictive of the ranking in IC (and vice versa) (Figure 4b). Congruently, the presence of a significant EC links (after significance testing) captures significantly larger values of the corresponding IC links, and vice versa (Fig. 4e,f). Importantly, EC also allows retrieving the spatial structure of the channel-map response (Figure 3, Figure 4a). These results are particularly notable given the constraints of *in vitro* systems, where spontaneous activity is often sparse and organized in bursts, limiting the statistical power for causal inference. While the original *in vivo* application of the IC framework relied on Convergent Cross Mapping (CCM) [24] to extract causal flow, we find that more traditional EC metrics — previously considered suboptimal *in vivo* — are surprisingly effective *in vitro*. This suggests that the dynamics of dissociated cultures, considered their lower complexity, may be more amenable to EC estimation with information theoretic or correlation methods.

These findings imply that characterizing EC prior to stimulation can predict, at least to a good extent, the impact

of perturbations on the network (Figure 4d). This means that in order to elicit desired responses (such as higher activity in specific channels) one does not need to follow a trial-and-error approach where different channels are stimulated in search of the desired effect - a labor-intensive, time-consuming effort. Instead, one can identify a priori (i.e., before stimulation) the set of network nodes that will trigger the largest effects on the overall network. These will generally correspond to EC hubs, i.e., nodes with many outgoing effective connections. This might allow to significantly enhance the efficacy of current protocols aimed at inducing plasticity effects in the culture. In fact, harnessing plasticity to sculpt the network structure is a long-sought goal in the field [41, 42, 48, 49]. Currently, the only (inflexible) way to induce desired network properties is to structurally design the network, using lithographic techniques that modify the morphology of the cell culture, influencing the attachment and growth of the neural networks [50–52]. By optimizing the spatial pattern of stimulating electrodes ahead of stimulation onset, our approach may thus substantially advance the prospects of modifying the networks in a controlled way by leveraging their intrinsic plasticity.

While strong, the relation between IC and EC is not completely straightforward. First, our IC measure — based on the two-sided Kolmogorov-Smirnov distance — captures the magnitude but not the direction (sign) of the perturbation effect and it is compared with the absolute value of EC metrics. We explored a variant based on a signed, one-sided test to discriminate excitatory from inhibitory responses. However, this yielded poor correspondence with signed EC (e.g., SC and XCov without absolute values). In particular, EC measures inferred from spontaneous activity tend to identify primarily excitatory links, while IC responses frequently reflect inhibition. This asymmetry may arise from intrinsic differences in the dynamics governing spontaneous versus evoked activity and points to a biologically meaningful divergence between the two regimes (see Supplementary Information C.3). A possible future direction is to test whether different stimulation parameters — such as shorter duration, lower amplitude, or alternative frequency patterns — might evoke responses more comparable in polarity to the causal links inferred from spontaneous activity, potentially improving the match between signed IC and EC. Second, a closer inspection at the scatter plots (Figure 4d) reveals an asymmetric relation: when EC is large, so is IC, but the reverse is not true. A possible explanation is that IC between two channels may be more strongly influenced by polysynaptic pathways. The strong stimulation delivered, deterministically leading to repeated spiking of neurons close to the stimulated channel, may trigger equally strong effects downstream, reaching with high probability also neurons that are only indirectly connected to the stimulated ones. Instead, the quite moderate firing rates observed during spontaneous activity may render polysynaptic effects too weak to appreciably influence effective connections. This hypothesis is supported by the strong correlation found between IC and the EC SP length (Figure 3g,j), a metric accounting for indirect connections. Moreover, this hypothesis would also explain the different behavior of EC and IC as functions of the electrode distance. As shown in Fig. 5a,b, the EC decreases exponentially with distance, while the IC decreases only linearly. The exponential decrease is in line with the well-established Exponential Distance Rule (EDR) [53, 54] in the cortex. The linear decrease of IC may depend on reverberation provided by intermediate neurons, acting as a sort of 'relays' that prevent an exponential decay. Noticeably, the fact that EC and IC both decrease with distance cannot explain their relationship: by regressing out distance from both metric, the residual predictive power of EC remains highly significant (Figure 5). Given that the relationship between stimulation effects and the underlying structural connectivity is not straightforward [23]), future studies could leverage the EC/IC distinction to investigate the structure-function relationship in cultured neural networks. By analyzing how spatial anatomical organization constrains both direct and indirect connectivity patterns, it may be possible to better understand the interplay between physical architecture and functional dynamics within these systems. This is also well-suited for application to brain organoids, which exhibit functional neuronal circuitry and complex oscillatory dynamics, thereby extending its relevance to advanced human-derived in vitro

4. Materials and Methods

4.1. Equipment Description

MaxOne High-Density Multi-electrode Arrays (HD-MEAs; Maxwell Biosystems, AG, Switzerland; https://www.mxwbio.com/products/maxone-mea-system-microelectrode-array/) were employed in this study. Built on Complementary Metal-Oxide-Semiconductor (CMOS) technology, the MaxOne platform features 26,400 platinum electrodes and supports recordings from up to 1,024 channels at the same time. The setup allows up to 32 of the 1,024 available recording channels to be used for input stimulation. The MaxOne chamber is specifically designed for plating neuronal cultures, and the Recording Unit (RU), where the chip is inserted, is compatible with the humidified environment of the cell culture incubator.

The experimental setup consists of an incubator, a RU, a chip with cultivated neurons, a hub, and a computer equipped with software for interfacing with the measurement system. The RU is a portable platform, designed to securely hold the chip chamber and fit within the incubator. The chip platinum electrodes are distributed across a 3.85×2.10 mm^2 area, providing a high electrode density of 3,625 units/mm^2 with a center-to-center spacing of 17.5 μm between adjacent sites. The RU connects to a hub, which subsequently links to a computer. Communication between the computer and the measurement system is managed by the MaxOne Server, which functions as a backend to the licensed *MaxLab Live Scope V24.2* software. This software provides a Graphical User Interface (GUI) for controlling the measurement system and visualizing data. Through the

Application Programming Interface (API), users can access all features of the MaxOne HD-MEA, enabling customized workflows and integration with external environments in Python.

4.1.1. Software Platform

The platform operates as a real-time MEA control system, integrating and managing both the native *MaxLab Live Scope V24.2* software functionalities and our Python custom-developed features for stimulation, recording, and spike detection. We expanded on the capabilities offered by *MaxLab Live Scope V24.2* to include tailored stimulation protocols, flexible recording configurations, and customized data processing workflows. *MXWServer* serves as the backbone for integration, efficiently handling data acquisition from the MaxOne hardware, processing it, and coordinating stimulation commands to the MEA in real time. During the experiments, this setup supports both open- and closed-loop configurations, adaptable to the experimental requirements.

4.1.2. MEA Setup and Coating

The chip is integrated into the base of a round chamber with an internal diameter of 19 mm and a height of 8 mm, specifically designed to hold the culture medium. Few days before neuronal seeding, the microchips were sterilized by complete immersion in 70% ethanol (v/v) for 45 minutes, rinsed with sterile deionized water and hair-dried under a sterile laminar hood. Then, they were pre-incubated at 37°C in L15 medium (see paragraph 4.1.3). On the plating day, chips were rinsed with sterile deionized water and coated with 20 μg/ml poly-L-lysine (PLL, Merck) for two hours at room temperature to enhance neuronal adhesion. Following coating, the PLL solution was removed, and chips were dried.

4.1.3. Neuronal Plating and Maintenance

Primary hippocampal neurons cultures were prepared from rat embryos aged 18 - 20 days (E18 - E20), slightly adapting the protocol published in [55]. Briefly, hippocampi were dissected from the brain under a sterile laminar hood, and neurons were dissociated through incubation with 0.08% Trypsin-EDTA followed by gentle trituration. After a pre-plating step to reduce the amount of glial cells, 120,000 neurons/cm^2 were seeded on PLL-coated chips in 100 μl of L15 medium supplemented with 5% Fetal Bovine Serum (FBS) and 1% penicillin-streptomycin. After a 90-minute incubation at 37 °C in a 5% CO_2 atmosphere, Neurobasal medium enriched with 1% Glutamax-1 and 2% B27 was added to fill the entire culture chamber. Two-thirds of the medium were refreshed every 3-4 days. All media and reagents were from Gibco - Thermofisher Scientific.

4.2. Ethics Statement

Wistar rats (Charles River) were housed under standard environmental conditions at the Animal Research Facility of the Department of Biomedical Sciences, University of Padua, in compliance with Italian animal welfare regulations (authorization numbers 522/2018-PR and 709/2023-PR).

4.3. Experimental Data

The experiments were conducted using dissociated hippocampal neuron cultures between Days in Vitro (DIV) 23–33. During each experimental session, the HD-MEA chips (MaxOne, MaxWell Biosystems) were maintained in a humidified incubator at 37°C and 5% (v/v) CO_2 throughout all the experimental session. The chips were interfaced with a computer, enabling experiment control via the MaxLab Live Scope linked to custom Python scripts.

To identify the most active electrodes, we applied the *MaxLab Live Scope V24.2* Activity Scan Assay function, which selects $N \approx 1,024$ channels exhibiting the highest spike amplitudes from the 26,400 electrodes available. These selected electrodes constituted the "channel map" used for the experimental protocol and analyses. The chosen electrodes were grouped into clusters of nine adjacent channels arranged in a 3×3 grid. From this configuration, a subset of M electrodes was chosen for stimulation; details regarding the criteria for their selection are provided in subsequent sections.

Neural activity was sampled at 20 kHz, with online spike detection enabled by hardware-level filtering and real-time thresholding. Signals were filtered using a high-pass filter with a cutoff frequency of 300 Hz, and the spike detection threshold was set to five times the root mean square noise above baseline, in accordance with the manufacturer's guidelines.

In this work, we focused on estimating connectivity directly from the chosen channels, relying on online spike detection rather than spike sorting. This approach allowed for near real-time connectivity analysis, avoiding the computational overhead associated with offline spike sorting algorithms.

4.3.1. Experiment

To assess whether perturbation effects can be predicted from spontaneous activity, we employed a two-phase experimental protocol combining neuronal culture recording and stimulation.

In the first phase, the Activity Scan Assay identified the most active regions of the chip, establishing the N-channels map. We then recorded spontaneous activity for $T_{rec} = 30$ minutes. Spike-train data collected during this phase were used to compute the EC between channel pairs (Figure 1a) using three principal metrics: TE, SC and XCov (see Section 4.4 for details). In the second phase, we characterized the network's response to perturbations by delivering electrical stimulations from selected electrodes. Each stimulation cycle consisted of three steps: (i) a short recording period immediately before stimulation, (ii) the stimulation itself delivered from a single channel, and (iii) a post-stimulation recording period across the entire N-channel map (see Figure 1b, top left and central panels). The stimulation protocol for each electrode consisted of a train of positive-then-negative biphasic pulses [40] at 200 Hz lasting $T_{\text{stim}} = 120$ ms, with individual pulses having an amplitude of 300 mV (peak-to-peak 600 mV) and a total duration of

0.4 ms evenly split into positive and negative phases of 0.2 ms each. This intensity was chosen to reliably perturb network activity [40] while minimizing the likelihood of inducing long-term plasticity. Although electrical stimulation can elicit synaptic modifications under specific conditions — such as prolonged high-frequency trains [40] — our stimulation consisted of short, interleaved single-site trains spaced several seconds apart. Between consecutive stimulations, we allowed the network to recover for $T_{\text{inter stim}} = 4$ s (see Figure S1a in Supplementary Information 4.4.9 for the stimulation protocol scheme).

To obtain robust estimates of IC, defined as the direct measure of network responses to single-site perturbations [24] (see Section 4.3.2), we repeated this cycle $N_T = 200$ times for each stimulating channel. Given practical constraints—each set of 200 stimulation cycles plus recovery intervals required approximately 15 minutes per stimulation channel — it was not feasible to stimulate all $N \approx 1024$ channels. Therefore, we randomly selected a subset of $M = 20$–25 stimulation channels per experiment, providing sufficient network coverage to evaluate the predictive power of EC metrics under realistic experimental conditions.

To further minimize plasticity-related biases, stimulation trials were randomized and interleaved across the M selected channels (see Supplementary Information A.2 for a validation of network stability across the stimulation protocol and a control for plasticity-related effects). Specifically, rather than applying all N_T stimulations consecutively on a single channel, each trial consisted of one stimulation cycle per channel, executed in a randomized order (see Figure 1b top central panel). Thus, stimulations delivered to the same channel were adequately spaced in time, reducing cumulative plasticity effects and preserving the integrity of the measured network responses. Additional details on timing, sequence randomization, and artifact mitigation strategies are provided in Supplementary Information A.1.

4.3.2. Interventional Connectivity

To quantify how perturbing a given source channel i affects the activity of a target channel j, we compared the spiking activity of channel j before and after stimulation of i (Figure 1b, top central and top right panels). The activity was evaluated within immediately pre- and post-stimulation time-windows of equal duration $T_W = 500$ ms, chosen as the best compromise between obtaining sufficient data for robust IC estimation and preserving quasi-stationarity of neural activity within each window. To prevent contamination by stimulation artifacts, we excluded short intervals immediately adjacent to stimulation periods: the pre-stimulation window ended Δ_{pre} milliseconds before the stimulation began, and the post-stimulation window started Δ_{post} milliseconds after the stimulation offset (see Figure S1a and Table S1b in Supplementary Information). Each stimulation of channel i was repeated N_T times, resulting in multiple trials of pre- and post-stimulation recordings for channel j. These trials were used to generate two distinct spike-count distributions for j: one referred to the activity prior to stimulation and another to the activity following stimulation. To generate the spike count distributions, each time window of length T_W was divided into n_w bins of duration dt_w. For each trial, we counted the number of spikes in each bin, resulting in spike counts x_j for channel j across all the trials and all the time-bins within both pre- and post-stimulation windows. Aggregating these counts across all N_T trials yielded two histograms: $p(x_j|\text{no stim})$ and $p(x_j|\text{stim}i)$ respectively for pre- and post-stimulation time-windows. We then quantified the effect of stimulation from channel i to channel j by defining the IC metric as the statistical distance $\mathcal{D}$ between these two distributions:

$$IC_{i\to j} = \mathcal{D}\Big(p(x_j|\text{no stim})\,,\, p(x_j|\text{stim } i)\Big). \tag{1}$$

Among the available options for $\mathcal{D}$, we selected the Kolmogorov-Smirnov distance, which ranges from 0 (identical distributions) to 1 (completely distinct distributions). Additionally, we performed a two-sided significance test (threshold $\alpha = 0.05$) to determine whether the observed IC value was statistically significant under the null hypothesis of identical pre- and post-stimulation distributions.

The IC matrix was constructed by computing $IC_{i\to j}$ for all source-target pairs, resulting in an $M \times N$ array, where - as previously introduced - M is the number of stimulation channels and N is the number of recording channels. In this work, we set the window length $T_W = 500$ ms, with exclusion intervals $\Delta_{\text{pre}} = 10$ ms and $\Delta_{\text{post}} = 5$ ms, and a bin size of $dt_w = 100$ ms. However, our results regarding the consistency between EC and IC remain robust against variations of these parameters, as detailed further in Supplementary Information A.3 and B. A summary of all parameter values used in our experiments and analyses is provided in Table S1b.

4.4. Effective Connectivity

This study evaluates the ability of various EC metrics to predict the effects of targeted perturbations on neuronal networks. Here, EC is defined following Wiener's (1956) definition of causality: a variable is considered "causal" if knowledge of its past improves the prediction of another variable's future, beyond what could be inferred from the variables own history alone [25, 26]. Accordingly, we constructed a directed network of causal interactions based on temporal dependencies observed in spontaneous neural dynamics.

To estimate EC, we used spike-trains recorded during $T_{rec} = 30$ minutes of spontaneous activity in the first phase of the experiment (Figure 1a). Spike times were binned into intervals of size $b = 0.3$ ms.EC was computed from the binarized spike trains, for each channel pair (i, j), producing an $N \times N$ connectivity matrix (Figure 6a-g). For direct validation against the experimentally derived IC matrix, the EC matrix was then reduced to an $M \times N$ subset, including only those links corresponding to the IC.

EC was estimated using three main metrics: delayed TE, SC, and XCov. Below, we briefly describe each metric and its computation.

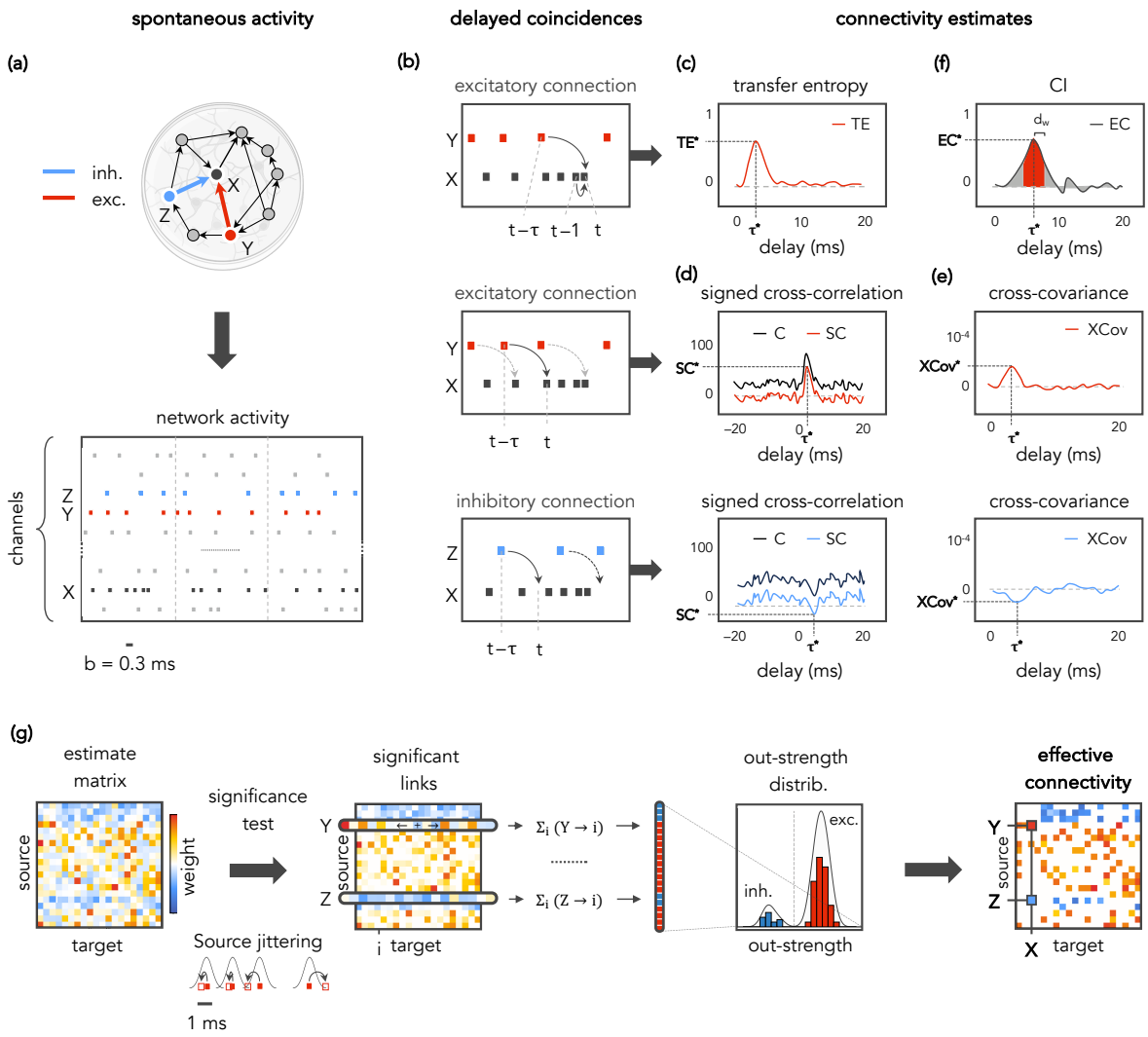

Figure 6: Illustration of Effective Connectivity estimation from spontaneous activity using delayed EC metrics (TE, SC, XCov) and significance testing. **(a) Upper panel**: schematic neuronal network illustrating an excitatory ($Y \to X$, red) and an inhibitory ($Z \to X$, blue) connection toward target neuron X. **Lower panel**: raster plot representing spike trains from multiple neurons, highlighting spikes from neurons X (black), Y (red), and Z (blue), discretized into bins of size $b = 0.3$ ms. **(b)** Illustration of spike-time coincidences used to compute EC metrics: *upper panel*, coincidences considered by TE between the current spike of target X (at time t) and past spikes of source Y (at delay τ), conditioned on X's immediate past spike ($t-1$). *Middle and lower panels*: spike-time coincidences used by SC and XCov, shown for excitatory ($Y \to X$, middle) and inhibitory ($Z \to X$, lower) connections. **(c)** Example plot of TE curve computed over delays, with peak value TE^* and optimal delay τ^* indicating the strongest causal influence from Y to X. **(d)** Example of cross-correlograms (black curve, C) and corresponding SC curves (colored curves, SC), illustrating baseline correction to distinguish excitatory (top, red) and inhibitory (bottom, blue) connections. The maximum absolute peak indicates connection strength (SC^*) at optimal delay (τ^*). **(e)** Cross-covariance ($XCov$) for an excitatory ($Y \to X$; top panel) and an inhibitory connection ($Z \to X$; bottom panel). **(f)** Calculation of the Coincidence Index (CI), defined as the integral of the EC curve within a temporal neighborhood ($\tau_w = 1.5$ ms) around the peak (τ^*), divided by the integral of the EC curve over the entire delay range. **(g)** Effective connectivity estimation process. First, the connectivity measure is computed for each neuron pair (excluding autapses). A significance test is then applied using a null model generated by randomly shifting the source neuron's spike times. From the resulting significant connectivity matrix, each source neuron's out-strength is calculated by summing its outgoing connection weights. A threshold is determined as the minimum point between the two peaks in the bimodal out-strength distribution. Neurons are classified as excitatory or inhibitory based on whether their out-strength lies above or below this threshold, and connections that conflict with the source neuron's classification are set to zero, yielding the final effective connectivity matrix.

4.4.1. Rationale for Choosing EC Metrics

The three EC metrics (delayed TE, SC, and XCov) were selected to capture complementary aspects of causal interactions and provide a robust validation framework. TE is a model-free, information-theoretic measure that makes no assumptions about the underlying data distribution, capturing nonlinear as well as linear dependencies between spike trains. In contrast, SC and XCov assume linear interactions between neuronal spike trains, with differences in their normalization methods: SC explicitly corrects for the expected baseline coincidence due to firing rates, distinguishing excitatory and inhibitory influences, whereas XCov quantifies linear time-lagged correlations by subtracting the expected number of coincidences under independence. Thus, TE allows for the detection of general, possibly nonlinear causal interactions, while SC and XCov specifically isolate linear, rate-driven interactions, differing primarily in their methods for baseline correction and sensitivity to firing rate fluctuations.

4.4.2. Delayed Transfer Entropy

Delayed TE quantifies the directed information flow between a sender channel Y and a target channel X (Figure 6b,c). It quantifies how knowledge of the past state of Y at a given time lag τ ($y_{t-\tau}$) reduces uncertainty about the current state of X (x_t), beyond what is explained by the target's own immediate past (x_{t-1}). Delayed TE is formally defined as [26, 38]:

$$TE_{Y\to X}(\tau) = I(x_t : y_{t-\tau}|x_{t-1}) = \\ = \sum p(x_t, x_{t-1}, y_{t-\tau}) \log_2 \frac{p(x_t|x_{t-1}, y_{t-\tau})}{p(x_t|x_{t-1})}. \quad (2)$$

In this work, TE was calculated over delays ranging from b to $\tau_{max} = 5$ ms, in increments of size b. The maximum TE value, $TE^*_{Y\to X} = \max_{\tau\in[b,\tau_{max}]\,\mathrm{ms}} \left\{ TE_{Y\to X}(\tau) \right\}$, provided an estimate of the connection strength, while the corresponding delay τ^* indicated the estimated communication delay from Y to X.

4.4.3. Signed Cross-correlation

SC [35] discriminates between excitatory and inhibitory connections by measuring the difference between the cross-correlogram at each delay and its mean value computed across delays(Figure 6d). For channels X and Y, SC is defined as:

$$SC_{Y\to X}(\tau) = C_{Y\to X}(\tau) - \mathrm{E}[C_{Y\to X}(\tau')], \quad (3)$$

where $C_{Y\to X}(\tau) = \sum_t x_t \cdot y_{t-\tau}$ counts delayed spike coincidences between x_t and y_t, with time shift τ, within the interval $[-\tau_{max}, \tau_{max}]$, divided in bins of size b, with $\tau_{max} =$ 5 ms. $\mathrm{E}[C_{Y\to X}(\tau')]$ is the mean count over delays within $[-\tau_{\max}, \tau_{\max}]$, with timestep b. This normalization removes the baseline of coincidences expected by chance, given firing rates, thereby highlighting excitatory ($SC > 0$) and inhibitory ($SC < 0$) connections. The connection strength $SC^*_{Y\to X}$ and corresponding delay τ^* were determined from the maximum absolute SC peak. Further details can be found in [35].

4.4.4. Cross Covariance

XCov captures time-lagged dependencies between neurons by measuring the cross-covariance between the state of channel X and the lagged state of Y:

$$\mathrm{XCov}_{Y\to X}(\tau) = \mathrm{E}[x_t \cdot y_{t-\tau}] - \mathrm{E}[x_t]\mathrm{E}[y_{t-\tau}], \quad (4)$$

where τ is the considered time-lag (Figure 6e). Similar to TE, XCov was computed for delays ranging from b to $\tau_{max} =$ 5 ms in increments of size b. The term $\mathrm{E}[x_t] \cdot \mathrm{E}[y_{t-\tau}]$ acts as sort of 'null model', representing the expected number of coincidences between X and Y occurring under X and Y independence. By subtracting this 'null model' count, XCov highlights the dependency between X and Y beyond what would be expected by chance alone. The peak XCov value, $\mathrm{XCov}^*_{Y\to X}$, at delay τ^*, was used as the estimate of connection strength.

4.4.5. Alternative Assessment of Connectivity

In addition to evaluating connection strengths by peak values, we introduced the Coincidence Index (CI) [56, 57], defined as the relative prominence of the EC peak with respect to baseline fluctuations. For each link $i \to j$, the CI was computed by considering a temporal neighborhood of radius $\tau_w = 1.5$ms around the peak delay τ^* of the EC function $EC_{i\to j}(\tau)$. Specifically we calculated the integral of the EC function within this neghborhood (Figure 6f), and divided it by the integral computed over the entire delay range $[-\tau_{max}; \tau_{max}]$:

$$\mathrm{EC}_{CI_{i\to j}} = \frac{\sum_{\tau=\tau^*-\tau_w}^{\tau^*+\tau_w} EC_{i\to j}(\tau)}{\sum_{\tau\in\text{all delays}} EC_{i\to j}(\tau)}. \quad (5)$$

Measurements calculated with this approach are denoted with the subscript "CI".

4.4.6. Significance Test

To assess the significance of EC estimates, we employed a null model designed to control for spurious coincidences, intrinsically caused by firing rates. This involved jittering the spike times of the source channel using a Gaussian distribution with a standard deviation of 1 ms (Figure 6g). This jittering disrupted systematic temporal dependencies while preserving essential properties of the source, such as spike rate and burst patterns. The spike times of the target channel were left unchanged to maintain the self-predictive structure of the receiver. For each channel pair, EC metrics (TE, SC, XCov, and their CI variants) were recalculated from 1000 jittered trials. Connections were considered significant if fewer than 1 of 1000 null-model values exceeded the observed connection strength (two-sided, $\alpha = 0.001$) [38]. Non-significant connections were set to zero. Measures having undergone this significance test thresholding are indicated with the subscript "s" (e.g., TE_s). For a fair comparison, the same identical jitter test was applied at the same time for all the metrics used (i.e. we used the same jittered spike times for the significant test of each EC measure).

4.4.7. Normalization of EC Metrics

To control for firing-rate effects, EC metrics were normalized (z-scored) relative to their respective jittered null-model distributions. Resulting z-scored metrics (denoted by subscript "Z") quantify how many standard deviations each observed EC value deviates from the mean of its null model, providing standardized, firing-rate independent connectivity strengths.

4.4.8. Shortest Path Analysis

To assess indirect connectivity within the neuronal network, we computed the Shortest Path (SP) between all pairs of channels from the complete $N \times N$ EC matrix. The distance between each pair of nodes (i, j) was defined as the inverse of the absolute EC weight connecting them, $d_{i,j} = |w_{\mathrm{EC}_{i,j}}|^{-1}$. Using this metric, stronger EC weights correspond to shorter distances, thus defining effective proximity in the inferred causal network.

SPs were calculated using Dijkstra's algorithm [58], producing an $N \times N$ SP matrix. To enable direct comparison with experimental IC values, the resulting SP matrices were subsequently reduced to an $M \times N$ format, retaining only paths originating from the M stimulation channels to all recording channels.

4.4.9. Spatial Correction for Connectivity Measures

To separate genuine connectivity effects from those influenced solely by spatial proximity, we implemented a spatial correction procedure on both IC and EC metrics. This procedure involved fitting each measure as a function of channel-to-channel distance ($\mathbf{d}$) using an exponential decay model defined by the following equations:

$$\mathbf{f}(\mathbf{IC}) = a_{IC} \cdot e^{-b_{IC} \cdot \mathbf{d}} + c_{IC} + \epsilon_{\mathbf{IC}} \tag{6}$$

$$\mathbf{f}(\mathbf{EC}) = a_{EC} \cdot e^{-b_{EC} \cdot \mathbf{d}} + c_{EC} + \epsilon_{\mathbf{EC}} \tag{7}$$

Here, $\mathbf{f}(\mathbf{IC})$ and $\mathbf{f}(\mathbf{EC})$ represent the predicted IC and EC values, respectively; $\mathbf{d}$ is the Euclidean distance between channel pairs; and a, b, and c are parameters optimized through least-squares fitting. The terms $\epsilon_{\mathbf{IC}}$ and $\epsilon_{\mathbf{EC}}$ represent the residuals. After fitting these exponential-decay models, we obtained corrected measures of connectivity by subtracting the spatial predictions from the original values:

$$IC_{ij}^{corrected} = \epsilon_{\mathbf{IC}} \tag{8}$$

$$EC_{ij}^{corrected} = \epsilon_{\mathbf{EC}} \tag{9}$$

This procedure ensured that correlations between EC and IC were not driven purely by spatial proximity, allowing us to isolate genuine functional connectivity from distance-related artifacts.

Acknowledgments

E.T. was supported from MUR and EU-FSE through the PhD fellowship PON Research and Innovation 2014-2020 (D.M 1061/2021) XXXVII Cycle / Action IV.4 "Tematiche Innovazione". L.M. was partially supported by National Institutes of Health Awards R01NS118461, R01MH127375 and R01DA055439 and National Science Foundation CAREER Award 2238247. P.P. and S.V. were supported from NEUREKA project (EU H2020, FET, GA-863245). M.A. was supported by MUR, PRIN grant 2022HSKLK9, CUP C53D23000740006, within the project "Unveiling the role of low dimensional activity manifolds in biological and artificial neural networks".

Data and Code Availability

The computation of Effective Connectivity was performed using the fully documented software package (Matlab and C++) shared in the code repository `https://github.com/elisatentori/EC_calculation` (an extended version of the package originally developed by [26]).
The computation of Interventional Connectivity and the full analysis was performed using the package `https://github.com/elisatentori/causality`, released with this paper. Data are available upon reasonable request.

CRediT authorship contribution statement

Elisa Tentori: Conceptualization, Methodology, Software, Visualization, Project administration, Writing – original draft . **George Kastellakis:** Methodology, Software, Writing - review and editing . **Marta Maschietto:** Methodology, Writing - review and editing . **Alessandro Leparulo:** Methodology, Writing - review and editing. **Panayiota Poirazi:** Funding acquisition, Methodology, Writing - review and editing . **Luca Mazzucato:** Supervision, Conceptualization, Project administration, Writing - review and editing. **Michele Allegra:** Supervision, Conceptualization, Project administration, Writing - original draft. **Stefano Vassanelli:** Funding acquisition, Supervision, Conceptualization, Project administration, Writing - review and editing.

References

[1] J. M. Yau, G. C. DeAngelis, D. E. Angelaki, Dissecting neural circuits for multisensory integration and crossmodal processing, Philosophical Transactions of the Royal Society B: Biological Sciences 370 (2015) 20140203.

[2] A. Sanzeni, A. Palmigiano, T. H. Nguyen, J. Luo, J. J. Nassi, J. H. Reynolds, M. H. Histed, K. D. Miller, N. Brunel, Mechanisms underlying reshuffling of visual responses by optogenetic stimulation in mice and monkeys, Neuron 111 (2023) 1–17.

[3] K. Rakhshan, J. D. Schall, A. C. Huk, R. Kiani, Neural mechanisms underlying robust target selection in response to microstimulation of the oculomotor system, The Journal of Neuroscience 45 (2025) e2356232024.

[4] J. Soldado-Magraner, Y. Minai, B. M. Yu, M. A. Smith, Robustness of working memory to prefrontal cortex microstimulation, bioRxiv (2025).

[5] D. J. O'Shea, L. Duncker, W. Goo, X. Sun, S. Vyas, E. M. Trautmann, I. Diester, C. Ramakrishnan, K. Deisseroth, M. Sahani, K. V. Shenoy, Direct neural perturbations reveal a dynamical mechanism for robust computation, bioRxiv (2022).

[6] P. T. Sadtler, K. M. Quick, M. D. Golub, S. M. Chase, S. I. Ryu, E. C. Tyler-Kabara, B. M. Yu, A. P. Batista, Neural constraints on learning, Nature 512 (2014) 423–426.

[7] N. P. Shah, A. Phillips, S. Madugula, A. Sher, A. Litke, E. Chichilnisky, Precise control of neural activity using dynamically optimized electrical stimulation, eLife 13 (2024) RP83424.

[8] H. Y. Chau, K. D. Miller, Exact linear theory of perturbation response in a space- and feature-dependent cortical circuit model, bioRxiv (2024).

[9] E. Krook-Magnuson, C. Armstrong, M. Oijala, I. Soltesz, On-demand optogenetic control of spontaneous seizures in temporal lobe epilepsy, Nature Communications 4 (2013) 1376.

[10] U. Topalovic, S. Barclay, C. Ling, A. Alzuhair, W. Yu, V. Hokhikyan, H. Chandrakumar, D. Rozgic, W. Jiang, S. Basir-Kazeruni, S. L. Maoz, C. S. Inman, A. Bari, A. Fallah, D. Eliashiv, I. Fried, N. Suthana, D. Markovic, A wearable platform for closed-loop stimulation and recording of single-neuron and local field potential activity in freely moving humans, Nature Neuroscience (2023).

[11] M. E. Obien, K. Deligkaris, T. J. Bullmann, D. J. Bakkum, U. Frey, Revealing neuronal function through microelectrode array recordings, Frontiers in Neuroscience 8 (2015) 423.

[12] S. Ronchi, M. Fiscella, C. Marchetti, V. Viswam, J. Müller, U. Frey, A. Hierlemann, Single-cell electrical stimulation using cmos-based

high-density microelectrode arrays, Frontiers in neuroscience 13 (2019) 208.

[13] I. Colombi, T. Nieus, M. Massimini, M. Chiappalone, Spontaneous and perturbational complexity in cortical cultures, Brain Sciences 11 (2021).

[14] H. Yamamoto, F. P. Spitzner, T. Takemuro, V. Buendía, H. Murota, C. Morante, T. Konno, S. Sato, A. Hirano-Iwata, A. Levina, V. Priesemann, M. A. Muñoz, J. Zierenberg, J. Soriano, Modular architecture facilitates noise-driven control of synchrony in neuronal networks, Science Advances 9 (2023) eade1755.

[15] T. Kobayashi, K. Shimba, T. Narumi, T. Asahina, K. Kotani, Y. Jimbo, Revealing single-neuron and network-activity interaction by combining high-density microelectrode array and optogenetics, Nature Communications 15 (2024) 9547.

[16] S. Tajima, T. Mita, D. J. Bakkum, H. Takahashi, T. Toyoizumi, Locally embedded presages of global network bursts in neuronal cultures, Proceedings of the National Academy of Sciences 114 (2017) 9517–9522.

[17] A. M. Houben, J. Garcia-Ojalvo, J. Soriano, Role of connectivity anisotropies in the dynamics of cultured neuronal networks, arXiv preprint arXiv:2501.04427 (2025).

[18] A. Ahtiainen, L. Leydolph, J. M. A. Tanskanen, A. Hunold, J. Haueisen, J. A. K. Hyttinen, Electric field temporal interference stimulation of neurons in vitro, Lab Chip 24 (2024) 3945–3957.

[19] R. Zhu, Z. Sun, C. Li, S. Ramakrishna, K. M. K. Chiu, L. He, Electrical stimulation affects neural stem cell fate and function in vitro, Experimental Neurology 319 (2019) 112963.

[20] S. Wu, Z. Wang, J. Wang, X. Wang, L. Xu, Y. Wang, Z. D. Xu, Chronic electrical stimulation induces functional network changes in cortical neuron cultures, Neuroscience Bulletin 36 (2020) 1295–1308.

[21] Y. Lu, Z. Wang, X. Li, Y. Wang, Y. Wang, X. Zhao, J. Zhang, J. Luo, Unveiling the impact of low-frequency electrical stimulation on network synchronization and learning behavior in cultured hippocampal neural networks, Brain Research 1810 (2024) 148163.

[22] F. Borra, S. Cocco, R. Monasson, Task learning through stimulation-induced plasticity in neural networks, PRX Life 2 (2024) 043014.

[23] S. Sadeh, C. Clopath, Theory of neuronal perturbome in cortical networks, Proceedings of the National Academy of Sciences 117 (2020) 26966–26976.

[24] A. Nejatbakhsh, F. Fumarola, S. Esteki, T. Toyoizumi, R. Kiani, L. Mazzucato, Predicting the effect of micro-stimulation on macaque prefrontal activity based on spontaneous circuit dynamics, Phys. Rev. Res. 5 (2023) 043211.

[25] N. Wiener, The theory of prediction, in: E. Beckenbach (Ed.), Modern Mathematics for Engineers, McGraw-Hill, New York, 1956.

[26] I. S., H. M.E., H. R., L. A., L. A.M., B. J.M., Extending transfer entropy improves identification of effective connectivity in a spiking cortical network model, in: PLoS One, 2011.

[27] F. K. J., Functional and effective connectivity in neuroimaging: A synthesis, Human Brain Mapping 2 (1994) 1–2.

[28] K. Schindler, M. Palus, M. Vejmelka, J. Bhattacharya, Causality detection based on information-theoretic approaches in time series analysis, Physics Reports 441 (2007) 1–46.

[29] C. Sun, K. Lin, C. Yeung, E. S. Ching, Y.-T. Huang, P.-Y. Lai, C. Chan, Revealing directed effective connectivity of cortical neuronal networks from measurements, Physical Review E 105 (2022) 044406.

[30] A. Pariz, Z. G. Esfahani, S. S. Parsi, A. Valizadeh, S. Canals, C. R. Mirasso, High frequency neurons determine effective connectivity in neuronal networks, NeuroImage 166 (2018) 349–359.

[31] R. Kobayashi, K. Kitano, Impact of network topology on inference of synaptic connectivity from multi-neuronal spike data simulated by a large-scale cortical network model, Journal of computational neuroscience 35 (2013) 109–124.

[32] F. Gerhard, T. Kispersky, G. J. Gutierrez, E. Marder, M. Kramer, U. Eden, Successful reconstruction of a physiological circuit with known connectivity from spiking activity alone, PLoS computational biology 9 (2013) e1003138.

[33] J. G. Orlandi, O. Stetter, J. Soriano, T. Geisel, D. Battaglia, Transfer entropy reconstruction and labeling of neuronal connections from simulated calcium imaging, PloS one 9 (2014) e98842.

[34] C. M., L. S., S. Panzeri, Inferring the temporal evolution of synaptic weights from dynamic functional connectivity, Brain Inf. 9 (2022) 28.

[35] V. Pastore, P. Massobrio, A. Godjoski, S. Martinoia, Identification of excitatory-inhibitory links and network topology in large-scale neuronal assemblies from multi-electrode recordings, PLOS Computational Biology 14 (2018) e1006381.

[36] S. Pawel, L. Kook, K. Reeve, Pitfalls and potentials in simulation studies: Questionable research practices in comparative simulation studies allow for spurious claims of superiority of any method, Biometrical Journal 66 (2024) 2200091.

[37] A. Das, I. R. Fiete, Systematic errors in connectivity inferred from activity in strongly recurrent networks, Nature Neuroscience 23 (2020) 1286–1296.

[38] P. Antonello, T. Varley, J. Beggs, M. Porcionatto, O. Sporns, J. Faber, Self-organization of in vitro neuronal assemblies drives to complex network topology, Elife (2022).

[39] D. A. Wagenaar, R. Madhavan, J. Pine, S. M. Potter, Controlling bursting in cortical cultures with closed-loop multi-electrode stimulation, Journal of Neuroscience 25 (2005) 680–688.

[40] Effective parameters for stimulation of dissociated cultures using multi-electrode arrays, Journal of Neuroscience Methods 138 (2004) 27–37.

[41] P. Massobrio, J. Tessadori, M. Chiappalone, M. Ghirardi, In vitro studies of neuronal networks and synaptic plasticity in invertebrates and in mammals using multielectrode arrays, Neural plasticity 2015 (2015) 196195.

[42] R. George, M. Chiappalone, M. Giugliano, T. Levi, S. Vassanelli, J. Partzsch, C. Mayr, Plasticity and adaptation in neuromorphic biohybrid systems, Iscience 23 (2020).

[43] F. Callegari, M. Brofiga, F. Poggio, P. Massobrio, Stimulus-evoked activity modulation of in vitro engineered cortical and hippocampal networks, Micromachines 13 (2022) 1212.

[44] L. Zullo, M. Chiappalone, S. Martinoia, F. Benfenati, A "spike-based" grammar underlies directional modification in network connectivity: effect on bursting activity and implications for bio-hybrids systems, PloS one 7 (2012) e49299.

[45] S. J. Ihle, S. Girardin, T. Felder, T. Ruff, J. Hengsteler, J. Duru, S. Weaver, C. Forró, J. Vörös, An experimental paradigm to investigate stimulation dependent activity in topologically constrained neuronal networks, Biosensors and Bioelectronics 201 (2022) 113896.

[46] B. M. Bader, A. Steder, A. B. Klein, B. Frølund, O. H. Schroeder, A. A. Jensen, Functional characterization of gabaa receptor-mediated modulation of cortical neuron network activity in microelectrode array recordings, PloS one 12 (2017) e0186147.

[47] J. H. Hyun, K. Nagahama, H. Namkung, N. Mignocchi, S. E. Roh, P. Hannan, S. Krüssel, C. Kwak, A. McElroy, B. Liu, M. Cui, S. Lee, D. Lee, R. L. Huganir, P. F. Worley, A. Sawa, H. B. Kwon, Tagging active neurons by soma-targeted cal-light, Nature Communications 13 (2022) 7692.

[48] D. A. Wagenaar, J. Pine, S. M. Potter, Searching for plasticity in dissociated cortical cultures on multi-electrode arrays, Journal of Negative Results in BioMedicine 5 (2006).

[49] F. Franke, D. Jäckel, J. Dragas, J. Müller, M. Radivojevic, D. Bakkum, A. Hierlemann, High-density microelectrode array recordings and real-time spike sorting for closed-loop experiments: an emerging technology to study neural plasticity, Frontiers in neural circuits 6 (2012) 105.

[50] B. C. Wheeler, G. J. Brewer, Designing neural networks in culture, Proceedings of the IEEE 98 (2010) 398–406.

[51] E. Marconi, T. Nieus, A. Maccione, P. Valente, A. Simi, M. Messa, S. Dante, P. Baldelli, L. Berdondini, F. Benfenati, Emergent functional properties of neuronal networks with controlled topology, PloS one 7 (2012) e34648.

[52] M. Montalà-Flaquer, C. F. López-León, D. Tornero, A. M. Houben, T. Fardet, P. Monceau, S. Bottani, J. Soriano, Rich dynamics and functional organization on topographically designed neuronal networks in vitro, Iscience 25 (2022).

[53] N. T. Markov, M. Ercsey-Ravasz, D. C. Van Essen, K. Knoblauch, Z. Toroczkai, H. Kennedy, Cortical high-density counterstream architectures, Science 342 (2013) 1238406.

[54] M. Ercsey-Ravasz, N. T. Markov, C. Lamy, D. C. Van Essen, K. Knoblauch, Z. Toroczkai, H. Kennedy, A predictive network model of cerebral cortical connectivity based on a distance rule, Neuron 80 (2013) 184–197.

[55] M. M., G. S., M. Dal Maschio, S. M., V. S., Sodium channel β 2 subunit promotes filopodia-like processes and expansion of the dendritic tree in developing rat hippocampal neurons, Frontiers in Cellular Neuroscience 7 (2013).

[56] T. Tateno, Y. Jimbo, Activity-dependent enhancement in the reliability of correlated spike timings in cultured cortical neurons, Biological Cybernetics 80 (1999) 45–55.

[57] M. Chiappalone, M. Bove, A. Vato, M. Tedesco, S. Martinoia, Dissociated cortical networks show spontaneously correlated activity patterns during in vitro development, Brain Research 1093 (2006) 41–53.

[58] E. W. Dijkstra, A note on two problems in connexion with graphs, Numerische Mathematik 1 (1959) 269–271.